The Astrophysical Journal, 777:58 (12pp), 2013 November 1 doi:10.1088/0004-637X/777/1/58

THE ROLE OF MERGER STAGE ON GALAXY RADIO SPECTRA IN LOCAL INFRARED-BRIGHT STARBURST GALAXIES

Eric J. Murphy
Infrared Processing and Analysis Center, California Institute of Technology, MC 220-6, Pasadena, CA 91125, USA; emurphy@ipac.caltech.edu
and
Observatories of the Carnegie Institution for Science, 813 Santa Barbara Street, Pasadena, CA 91101, USA
Received 2013 June 5; accepted 2013 August 15; published 2013 October 17

ABSTRACT

An investigation of the steep, high-frequency (i.e., $\nu \sim 12$ GHz) radio spectra among a sample of 31 local infrared-bright starburst galaxies is carried out in light of their *Hubble-Space-Telescope*-based merger classifications. Radio data covering as many as 10 individual bands allow for spectral indices to be measured over three frequency bins between 0.15 and 32.5 GHz. Sources having the flattest spectral indices measured at ∼2 and 4 GHz, arising from large free–free optical depths among the densest starbursts, appear to be in ongoing through post-stage mergers. The spectral indices measured at higher frequencies (i.e., ∼12 GHz) are steepest for sources associated with ongoing mergers in which their nuclei are distinct, but share a common stellar envelope and/or exhibit tidal tails. These results hold after excluding potential active galactic nuclei based on their low 6.2 μm polycyclic aromatic hydrocarbon equivalent widths. Consequently, the low-, mid-, and high-frequency spectral indices each appear to be sensitive to the exact merger stage. It is additionally shown that ongoing mergers, whose progenitors are still separated and share a common envelope and/or exhibit tidal tails, also exhibit excess radio emission relative to what is expected given the far-infrared/radio correlation, suggesting that there may be a significant amount of radio emission that is not associated with ongoing star formation. The combination of these observations, along with high-resolution radio morphologies, leads to a picture in which the steep high-frequency radio spectral indices and excess radio emission arise from radio continuum bridges and tidal tails that are not associated with star formation, similar to what is observed for so-called "taffy" galaxies. This scenario may also explain the seemingly low far-infrared/radio ratios measured for many high-z submillimeter galaxies, a number of which are merger-driven starbursts.

Key words: galaxies: active – galaxies: starburst – infrared: galaxies – radio continuum: galaxies – stars: formation

Online-only material: color figure

1. INTRODUCTION

Encoded in the radio spectra of star-forming galaxies, which are typically well characterized by a power law ($S_\nu \propto \nu^{-\alpha}$), lies information on the thermal and non-thermal energetic processes powering them. Both thermal and non-thermal emission processes are typically associated with massive star formation, underlying the basis for the well-known far-infrared (FIR)/radio correlation (de Jong et al. 1985; Helou et al. 1985; Condon 1992). FIR emission arises from re-radiated UV/optical photons that heat dust grains surrounding massive star-forming regions. The young, massive O/B stars in such regions, whose lifetimes are $\lesssim$10 Myr, produce ionizing radiation that is proportional to the amount of free–free emission. Stars more massive than $\gtrsim$8 $M_\odot$ end their lives as supernovae (SNe), whose remnants (supernova remnants, SNRs) are thought to be the primary accelerators of cosmic-ray (CR) electrons, which emit synchrotron emission as they propagate through a galaxy's magnetized interstellar medium (ISM).

The non-thermal emission typically dominates the free–free emission at frequencies $\lesssim$30 GHz (Condon 1992), having a relatively steep spectrum (i.e., $\alpha \approx 0.83$; Niklas et al. 1997). Thermal bremsstrahlung (free–free) emission, on the other hand, has a much flatter spectrum ($\alpha \approx 0.1$), making it difficult to separate this component from the non-thermal emission. Thus, at frequencies $\gtrsim$30 GHz, where the thermal fraction starts to become large, radio observations should become robust measures for the ongoing star formation rate in galaxies (Murphy et al. 2011b, 2012). However, this has been shown to not necessarily be the case for a number of local luminous infrared galaxies (LIRGs), whose IR (8–1000 μm) luminosities exceed $L_{\rm IR} \gtrsim 10^{11}\ L_\odot$.

In a number of these IR-bright starbursts, their high-frequency (i.e., $\gtrsim$10 GHz) radio spectra are much steeper than expected for an increased thermal fraction, and in some cases they even show possible evidence for spectral steepening (Clemens et al. 2008, 2010; Leroy et al. 2011). Understanding the physical underpinnings driving this behavior can greatly help with the interpretation of radio observations for higher redshift starbursts, which is important given that IR-luminous galaxies appear to be much more common in the early universe and dominate the star formation rate density in the redshift range spanning $1 \lesssim z \lesssim 3$, being an order of magnitude larger than today (e.g., Chary & Elbaz 2001; Le Floc'h et al. 2005; Caputi et al. 2007; Murphy et al. 2011a; Magnelli et al. 2013).

In the local universe, it is well known that LIRGs and ultraluminous LIRGs (ULIRGs; $L_{\rm IR} \gtrsim 10^{12}\ L_\odot$) appear to be undergoing an intense starburst phase. Within these systems are compact star-forming regions that have been triggered predominantly through major mergers (see, e.g., Armus et al. 1987, 1988, 1989, 1990; Sanders et al. 1988a, 1988b; Murphy et al. 1996; Veilleux et al. 1995, 1997, 2002). Major mergers have the ability to significantly complicate the interpretation of observed radio properties when individual systems are not resolved, the classic case being the so-called "taffy" galaxies (Condon et al. 1993, 2002). When unresolved, the systems appear to have nearly a factor of ∼2 more radio continuum emission relative to what is expected given the FIR/radio correlation, as well as unusually steep (i.e., $\alpha \approx 1.0$) radio spectra. However, when resolved, it is clearly found that the

Table 1
Radio and Infrared Properties of the Sample Galaxies

Galaxy	Dist.[a] (Mpc)	$L_{IR}/10^{11}$ [a] ($L_\odot$)	$F_{FIR}/10^{-13}$ [b] (W m^{-2})	$q_{1.4\,GHz}$[c] (dex)	$q_{8.4\,GHz}$[c] (dex)	6.2 μm EQW[d] (μm)	$s_{9.7\mu m}$[d]	Merger Stage[e]
NGC 34	84.1	3.09	7.69	2.49	3.13	0.45/SF	−0.79	5
IC 1623	85.5	5.13	11.18	2.08	2.74	0.30/SF[f]	−0.98[f]	3
CGCG 436−030	134.0	4.90	4.70	2.40	2.99	0.35/SF	−1.10	2
IRAS F01364−1042	210.0	7.08	3.02	2.71	2.99	0.39/SF	−1.27	5
IRAS F01417+1651	119.0	4.37	5.74	2.58	2.89	...	...	3
UGC 2369	136.0	4.68	3.94	2.33	2.90	0.57/SB	−0.11	2
IRAS F03359+1523	152.0	3.55	2.88	2.60	2.84	...	...	3
NGC 1614	67.8	4.47	14.62	2.45	2.98	0.61/SB	−0.41	5
IRAS F05189−2524	187.0	14.45	5.89	2.74	3.14	0.03/AGN	−0.29	6
NGC 2623	84.1	4.37	11.02	2.49	2.92	0.27/AGN	−1.12	5
IRAS F08572+3915	264.0	14.45	2.97	3.27	3.29	0.03/AGN	−3.58	4
UGC 04881	178.0	5.45	3.22	2.37	2.99	0.47/SF[g]	−0.63[g]	2
UGC 05101	177.0	10.23	6.28	1.99	2.50	0.13/AGN	−0.78	5
IRAS F10173+0828	224.0	7.24	2.58	2.84	3.10	0.35/SF	−1.20	0
IRAS F10565+2448	197.0	12.02	5.84	2.44	3.04	0.51/SF	−0.75	2
MCG +07-23-019	158.0	4.17	3.23	2.37	2.87	0.64/SB	−0.55	2
IRAS F11231+1456	157.0	4.37	3.23	2.65	3.22	0.60/SB	−0.22	1
NGC 3690	50.8	8.42	47.24	2.26	2.71	0.23/AGN[g]	−1.15[g]	3
IRAS F12112+0305	340.0	22.91	4.02	2.66	3.03	0.30/SF	−1.24	4
UGC 08058	192.0	37.15	14.22	2.14	2.30	0.01/AGN	−0.48	...
UGC 08387	110.0	5.37	8.18	2.32	2.80	0.62/SB	−1.01	4
NGC 5256 S	129.0	3.09	3.78	1.90	2.62	0.44/SF	−0.47	3
UGC 08696	173.0	16.22	9.75	2.25	2.78	0.12/AGN	−1.37	5
IRAS F14348−1447	387.0	24.55	3.12	2.37	2.89	0.25/AGN	−1.36	4
IRAS F15163+4255	183.0	8.32	4.34	2.36	2.91	0.75/SB	0.32	4
IRAS F15250+3608	254.0	12.02	3.11	2.76	2.90	0.03/AGN	−2.69	5
UGC 09913	87.9	19.05	47.92	2.59	2.94	0.17/AGN	−2.26	5
NGC 6286 S	85.7	1.62	5.08	1.94	2.63	0.59/SB	−0.40	...
NGC 7469	70.8	4.47	13.31	2.29	2.85	0.23/AGN	0.06	2
IC 5298	119.0	3.98	4.46	2.53	3.16	0.12/AGN	−0.37	0
MRK 331	79.3	3.16	8.71	2.52	3.02	0.63/SB	−0.35	1

Notes.
[a] Distances and total IR (8–1000 μm) luminosities are taken from Armus et al. (2009).
[b] *IRAS*-based FIR (42.5–122.5 μm) fluxes taken from Clemens et al. (2008), where $(F_{FIR}/\mathrm{W\,m^{-2}}) = 1.26 \times 10^{-14}\,[2.58\,f_\nu(60\,\mu\mathrm{m}) + f_\nu(100\,\mu\mathrm{m})/\mathrm{Jy}]$.
[c] Logarithmic ratio of FIR-to-radio emission given in Clemens et al. (2008), where $q_\nu = \log(F_{FIR}/3.75 \times 10^{12}\,\mathrm{W\,m^{-2}}) - \log(S_\nu/\mathrm{W\,m^{-2}\,Hz^{-1}})$.
[d] 6.2 μm PAH EQWs and silicate strengths ($s_{9.7\mu m}$) are taken from Stierwalt et al. (2013). AGN and starburst (SB) dominated galaxies, based on having 6.2 μm PAH EQWs below and above 0.27 and 0.54 μm, respectively, are identified. All systems with 6.2 μm PAH EQWs above 0.27 μm are considered to be star formation (SF) dominated.
[e] The merger stage as derived from the high-resolution *HST* data (0 = non-merger, 1 = pre-merger, 2 = ongoing merger with separable progenitor galaxies, 3 = ongoing merger with progenitors sharing a common envelope, 4 = ongoing merger with double nuclei plus tidal tail, 5 = post-merger with single nucleus plus prominent tail, and 6 = post-merger with single nucleus and a disturbed morphology), as described in Haan et al. (2011).
[f] Mid-IR spectroscopy only available for the eastern component.
[g] Luminosity-weighted average of mid-IR measurements from individual galaxy nuclei.

integrated radio properties are driven by radio continuum emission that forms a bridge connecting the galaxy pairs; the radio continuum emission in the bridges is characterized by a steep spectrum and is roughly equal to that in the individual galaxies, which have radio spectral indices and FIR/radio ratios typical of normal spiral galaxies (Condon et al. 1993, 2002).

In this paper, an explanation is presented for occurrences of steep radio spectra observed in local ULIRGs within the context of their merger stage. The paper is organized as follows. In Section 2 the sample and data used in the analysis are presented. The major results are described in Section 3, and then discussed in Section 4 to piece together a self-consistent picture describing the radio properties for this sample of local starbursts. Finally, the main conclusions are summarized in Section 5.

2. DATA AND ANALYSIS

The galaxy sample being analyzed here is drawn from sources in the *IRAS* revised Bright Galaxies Sample (Soifer et al. 1989; Sanders et al. 2003) having 60 μm flux densities larger than 5.24 Jy and FIR (42.5–122.5 μm) luminosities $\geqslant 10^{11.25}\,L_\odot$. The 40 systems that meet these criteria were originally imaged by Condon et al. (1991) at 8.4 GHz with 0.″25 resolution. For 31 of these sources, Clemens et al. (2008) presented additional new Very Large Array (VLA) 22.5 GHz data (obtained in D-configuration), along with new 8.4 GHz data for seven objects (obtained in C-configuration) and archival observations to increase the radio spectral coverage of each system. Additional lower frequency data at 244 and 610 MHz were obtained and presented in Clemens et al. (2010), and for 14 and 13 sources existing 6.0 and 32.5 GHz measurements, respectively, from Leroy et al. (2011) are used. The present analysis focuses on these 31 galaxies (see Table 1) having well-sampled radio spectra between 0.15 and 32.5 GHz (typically 6 bands with as many as 10 including some combination of data observed at 0.151, 0.244, 0.365, 0.610, 1.4, 4.8, 6.0, 8.4, 15.0, 22.5, and 32.5 GHz). While these radio data span over

an order of magnitude in frequency and have varying spatial resolutions, missing short-spacing data will not significantly affect the results given that the highest frequency radio data should be sensitive to $\gtrsim 1'$ angular scales, much larger than the typical emitting regions for this sample of IR-bright galaxies.

For NGC 3690, UGC 08387, UGC 08696, and IRAS F15163+4255, the 22.5 GHz flux densities of Clemens et al. (2008) are significantly lower than the 32.5 GHz flux densities presented in Leroy et al. (2011). These discrepancies may be associated with the difficulties of measuring flux densities through the pressure-broadened 22.3 GHz line of atmospheric water vapor, and therefore the 22.5 GHz flux densities for these four sources are not included in the present analysis. Additionally, the 15 GHz flux density for UGC 08387, which was reduced from archival VLA data by Clemens et al. (2008), is found to be discrepant with the combination of lower frequency radio data and the 32.5 GHz flux density of Leroy et al. (2011) and is therefore not used. For IRAS F15163+4255, the 4.8 GHz flux density measured by Gregory & Condon (1991) using the 91 m telescope in Green Bank is found to be significantly discrepant with the 6.0 GHz flux density of Leroy et al. (2011) and is dropped from the analysis as well.

IRAS-based FIR fluxes and logarithmic FIR-to-radio ratios at 1.4 and 8.4 GHz, each of which were reported in Clemens et al. (2008), are also used in the analysis. The FIR flux, $F_{\rm FIR}$, is estimated using *IRAS* 60 and 100 μm flux densities and the relation given by Helou et al. (1985) such that

$$\left(\frac{F_{\rm FIR}}{\rm W\,m^{-2}}\right) = 1.26\times10^{-14}\left[\frac{2.58\,f_\nu(60\,\mu{\rm m}) + f_\nu(100\,\mu{\rm m})}{\rm Jy}\right]. \quad (1)$$

Logarithmic $F_{\rm FIR}$/radio ratios at frequency ν are also defined using the relation given by Helou et al. (1985) such that

$$q_\nu = \log\left(\frac{F_{\rm FIR}}{3.75\times10^{12}\,\rm W\,m^{-2}}\right) - \log\left(\frac{S_\nu}{\rm W\,m^{-2}\,Hz^{-1}}\right). \quad (2)$$

Each of these values is given in Table 1 for each source.

The mid-IR spectral properties were collected by the *Spitzer* Infrared Spectrograph (IRS; Houck et al. 2004) as part of the Great Observatories All-Sky LIRG Survey (GOALS; Armus et al. 2009) and are taken from Stierwalt et al. (2013). For two sources, IRS observations missed the nucleus of the galaxy (IRAS F01417+1651, IRAS F03359+1523). In the analysis 6.2 μm polycyclic aromatic hydrocarbon (PAH) equivalent widths (EQWs) and 9.7 μm silicate strengths (see Stierwalt et al. 2013) are used. Similar to Murphy et al. (2013), the measured 6.2 μm PAH EQWs are used as an active galactic nuclei (AGN) discriminant. Sources hosting AGNs typically have very small PAH EQWs (e.g., Genzel et al. 1998; Armus et al. 2007). Specifically, starburst-dominated systems appear to have 6.2 μm PAH EQWs that are $\gtrsim$0.54 μm (Brandl et al. 2006), while AGNs have 6.2 μm PAH EQWs that are $\lesssim$0.27 μm. In this paper it is assumed that all sources having PAH EQWs $\geqslant$0.27 μm are primarily powered by star formation. Given that the PAH EQW is used as an AGN discriminant, we exclude both sources missing IRS data in the present analysis when focusing on star-formation-dominated systems. The silicate strength at 9.7 μm is defined as $s_{9.7\,\mu{\rm m}} = \log(f_{9.7\,\mu{\rm m}}/C_{9.7\,\mu{\rm m}})$, where $f_{9.7\,\mu{\rm m}}$ is the measured flux density at the central wavelength of the absorption feature and $C_{9.7\,\mu{\rm m}}$ is the expected continuum level in the absence of the absorption feature. For two sources (UGC 04881 and NGC 3690), IR luminosity-weighted averages of individual IRS measurements from each nucleus are used.

This analysis additionally makes use of merger classifications based on available *Hubble Space Telescope* (*HST*) imaging for 29 galaxies taken as part of an *HST*/Advanced Camera for Surveys (ACS) survey of the GOALS sample (Kim et al. 2013; A. S. Evans et al. 2014, in preparation). The merger classifications were assigned using both *HST* optical [i.e., ACS *B* band (F435W) and *I* band (F814W)] and near-IR [i.e., Near-Infrared Camera and Multi-Object Spectrometer *H*-band (F160W)] imaging. The individual merger stages are classified by an integer value ranging from 0 to 6 and are described in detail by Haan et al. (2011). Briefly, the numerical classifications are defined in the following way: 0 = non-merger, 1 = pre-merger, 2 = ongoing merger with separable progenitor galaxies, 3 = ongoing merger with progenitors sharing a common envelope, 4 = ongoing merger with double nuclei plus tidal tail, 5 = post-merger with single nucleus plus prominent tail, and 6 = post-merger with single nucleus and a disturbed morphology. For two sources, merger classifications are not available. *HST* data were not taken for NGC 6286, and the *HST*/ACS data saturated for the observations of UGC 08058 (Mrk 231). Each of these properties is given in Table 1.

3. RESULTS

A number of the IR-bright galaxies being investigated here are known to have high-frequency (i.e., $\gtrsim$10 GHz) radio spectra that are much steeper than expected given that the thermal fraction should increase with frequency and work to flatten the spectra (e.g., Clemens et al. 2008, 2010; Leroy et al. 2011). In the following section, correlations between various galaxy properties that may help to explain such steep, high-frequency radio spectral indices are investigated after removing potential AGNs from the sample using the mid-IR spectroscopic data. A number of physical considerations have already been put forth and discussed by Clemens et al. (2008), including those used to explain the high-frequency turnover in the starburst galaxy NGC 1569 by Lisenfeld et al. (2004), and we refer the reader to these papers. To summarize, these physical processes include synchrotron aging, stochastic events such as radio hypernovae, rapid temporal variations in the star formation rate, and the escape of low-energy CRs through convective transport. Each scenario has been found to be unsatisfactory for this sample of local starburst galaxies in a large part due to the extremely short (i.e., $\sim10^4$ yr; Condon et al. 1991) radiative lifetimes estimated for CR electrons in such systems, which requires a near continuous injection of particles.

3.1. Radio Spectral Curvature

The radio spectra of each source are broken up into low-, mid-, and high-frequency bins, so the spectral curvature of each source can be crudely measured. The low-frequency bin is defined as $\nu < 5$ GHz, the mid-frequency bin spans 1 GHz $< \nu <$ 10 GHz, and the high-frequency bin is defined as $\nu > 4$ GHz. This allows the radio spectral index to be calculated using typically three or more data points in each frequency bin (see exact numbers in Table 2). The spectral index is estimated by an ordinary least-squares fit over each frequency bin range, weighted by the photometric errors. Each spectral index is given in Table 2 along with uncertainties from the fitting. Additionally given in Table 2 is the average frequency, weighted by the signal-to-noise ratio of each photometric data point, over which the radio spectral index was calculated.

Table 2
Radio Spectral Indices

Galaxy	$\langle\nu_{\rm low}\rangle$[a] (GHz)	$\alpha_{\rm low}$[b]	$\langle\nu_{\rm mid}\rangle$[a] (GHz)	$\alpha_{\rm mid}$[b]	$\langle\nu_{\rm high}\rangle$[a] (GHz)	$\alpha_{\rm high}$[b]
NGC 34	4.05 (2)	0.70 ± 0.031	4.64 (3)	0.74 ± 0.029	10.83 (3)	0.87 ± 0.014
IC 1623	1.76 (3)	0.90 ± 0.057	6.05 (3)	0.85 ± 0.024	10.09 (3)	0.95 ± 0.087
CGCG 436−030	2.18 (2)	0.69 ± 0.085	4.63 (4)	0.74 ± 0.027	14.58 (5)	0.56 ± 0.037
IRAS F01364−1042	2.44 (2)	0.24 ± 0.089	5.07 (4)	0.34 ± 0.034	12.88 (5)	0.69 ± 0.045
IRAS F01417+1651	2.22 (2)	0.35 ± 0.085	4.13 (4)	0.35 ± 0.035	15.74 (6)	0.74 ± 0.037
UGC 2369	1.10 (3)	0.33 ± 0.079	3.04 (2)	0.73 ± 0.058	17.40 (2)	0.93 ± 0.117
IRAS F03359+1523	2.02 (3)	0.50 ± 0.073	3.58 (3)	0.34 ± 0.051	13.41 (3)	0.68 ± 0.073
NGC 1614	1.16 (4)	0.47 ± 0.044	7.12 (3)	0.68 ± 0.020	10.10 (3)	0.67 ± 0.048
IRAS F05189−2524	2.75 (2)	0.43 ± 0.051	3.73 (3)	0.46 ± 0.042	11.19 (3)	0.68 ± 0.051
NGC 2623	1.71 (3)	0.33 ± 0.084	3.24 (3)	0.53 ± 0.055	20.21 (3)	0.71 ± 0.075
IRAS F08572+3915	3.52 (3)	0.02 ± 0.081	5.62 (4)	0.02 ± 0.057	11.49 (5)	0.26 ± 0.047
UGC 04881	1.10 (3)	0.34 ± 0.084	4.03 (3)	0.75 ± 0.037	12.18 (4)	0.95 ± 0.092
UGC 05101	0.92 (5)	0.51 ± 0.031	4.16 (4)	0.70 ± 0.037	15.25 (6)	0.93 ± 0.047
IRAS F10173+0828	3.51 (3)	0.36 ± 0.063	4.77 (3)	0.38 ± 0.069	9.53 (4)	0.48 ± 0.065
IRAS F10565+2448	4.01 (4)	0.73 ± 0.022	4.53 (3)	0.77 ± 0.030	5.00 (2)	0.81 ± 0.179
MCG +07-23-019	2.50 (4)	0.72 ± 0.032	4.28 (4)	0.69 ± 0.032	12.79 (6)	0.57 ± 0.035
IRAS F11231+1456	1.17 (3)	0.47 ± 0.139	4.09 (2)	0.73 ± 0.038	11.84 (2)	0.63 ± 0.190
NGC 3690	0.89 (5)	0.61 ± 0.027	5.64 (4)	0.59 ± 0.034	12.52 (5)	0.69 ± 0.041
IRAS F12112+0305	3.62 (4)	0.37 ± 0.028	4.24 (3)	0.38 ± 0.029	9.86 (4)	0.73 ± 0.025
UGC 08058	3.39 (5)	0.14 ± 0.007	5.49 (4)	0.26 ± 0.007	10.07 (6)	0.51 ± 0.006
UGC 08387	1.06 (4)	0.50 ± 0.019	4.08 (4)	0.60 ± 0.035	11.52 (4)	0.67 ± 0.063
NGC 5256 S	1.44 (5)	0.72 ± 0.028	4.67 (3)	0.91 ± 0.030	11.53 (4)	0.66 ± 0.059
UGC 08696	0.89 (6)	0.59 ± 0.029	4.21 (4)	0.64 ± 0.037	13.38 (5)	0.74 ± 0.052
IRAS F14348−1447	1.29 (2)	-0.22 ± 0.244	3.26 (2)	0.67 ± 0.055	14.81 (2)	0.89 ± 0.147
IRAS F15163+4255	0.98 (3)	0.72 ± 0.053	4.26 (3)	0.68 ± 0.034	12.39 (3)	0.87 ± 0.075
IRAS F15250+3608	1.92 (2)	0.09 ± 0.190	4.40 (4)	0.14 ± 0.040	14.76 (6)	0.71 ± 0.051
UGC 09913	1.51 (4)	0.13 ± 0.033	4.06 (4)	0.37 ± 0.034	14.62 (6)	0.61 ± 0.041
NGC 6286 S	1.05 (5)	0.73 ± 0.033	4.35 (3)	0.89 ± 0.034	10.81 (3)	1.02 ± 0.123
NGC 7469	1.62 (3)	0.63 ± 0.042	6.29 (3)	0.71 ± 0.018	12.03 (3)	1.06 ± 0.031
IC 5298	2.38 (2)	0.74 ± 0.087	4.61 (3)	0.80 ± 0.035	13.53 (3)	0.80 ± 0.056
MRK 331	2.21 (2)	0.67 ± 0.085	4.35 (3)	0.65 ± 0.030	15.14 (3)	0.78 ± 0.045
Medians	1.76 (3)	0.50 ± 0.046	4.35 (3)	0.67 ± 0.040	12.39 (4)	0.71 ± 0.031

Notes.
[a] The average frequency, weighted by the signal-to-noise ratio of each photometric data point, over which the radio spectral index was calculated. The number in parentheses indicates how many frequencies were used in the calculation.
[b] Radio spectral indices, where $S_\nu \propto \nu^{-\alpha}$, measured in the following frequency bins using data from Clemens et al. (2010) and Leroy et al. (2011); low: $\nu < 5$ GHz, mid: 1 GHz $< \nu <$ 10 GHz, and high: $\nu > 4$ GHz.

In the top panel of Figure 1, the median spectral indices of each bin are plotted as a function of the median frequency over which the spectral indices were calculated. The median frequencies of the low-, mid-, and high-frequency bins are ≈2, 4, and 12 GHz, respectively. The horizontal error bar indicates the standard deviation in the average frequencies, while the vertical error bar is the error on the average spectral index. Average spectral indices are shown for the entire sample, as well as for starbursting and AGN-dominated systems, as defined by their 6.2 μm PAH EQWs (see Section 2).

While a rather clear distinction between the average radio spectral indices measured between 1.49 and 8.44 GHz (essentially the $\alpha_{\rm mid}$ presented here) was pointed out by Murphy et al. (2013), whereby AGN-dominated sources typically have a much flatter radio spectral index compared to starburst-dominated sources, the high-frequency radio spectral indices are statistically indistinguishable between both AGN- and starburst-dominated systems. Using the 6.2 μm PAH EQW to split the sources up into starburst and AGN-dominated systems, the median high-frequency radio spectral index for starburst-dominated systems is 0.78, with a standard deviation of 0.16. For the AGN-dominated systems, the median spectral index is 0.71, albeit with a slightly larger scatter of 0.20. Thus, the steep spectral indices at ∼12 GHz do not seem to be the result of radio emission associated with an AGN.

In the bottom panel of Figure 1, the average spectral indices in each frequency bin are plotted for only those sources whose energetics are thought to be dominated by star formation based on having a 6.2 μm PAH EQW $\geqslant$ 0.27 μm. The overplotted lines correspond to expectations based on four different radio spectra that are shown in Figure 2 to illustrate the change in radio spectral index as a function of frequency based on the increased thermal fraction toward higher frequencies for a normal star-forming galaxy. The radio-to-IR models are based on the physical description given in Murphy (2009), where the total IR (8–1000 μm) flux is set to $F_{\rm IR} = 10^{-9}$ W m^{-2} and the source is assumed to follow the FIR/radio correlation. The radio spectra are constructed following the prescription given in Murphy (2009), resulting in a non-thermal spectral index of ≈0.83 with 1.4 GHz thermal radio fractions of $f_{\rm T}^{1.4\,{\rm GHz}} \approx 5\%$ (dashed line), 10% (dotted line), and 15% (dot-dashed line). These 1.4 GHz thermal fractions correspond to 30 GHz thermal fractions of $f_{\rm T}^{30\,{\rm GHz}} \approx 33\%$, 51%, and 63%, respectively.

As pointed out by Clemens et al. (2008), and also seen by Leroy et al. (2011) using new 33 GHz VLA data, there is a clear trend of spectral flattening/steepening toward lower/higher

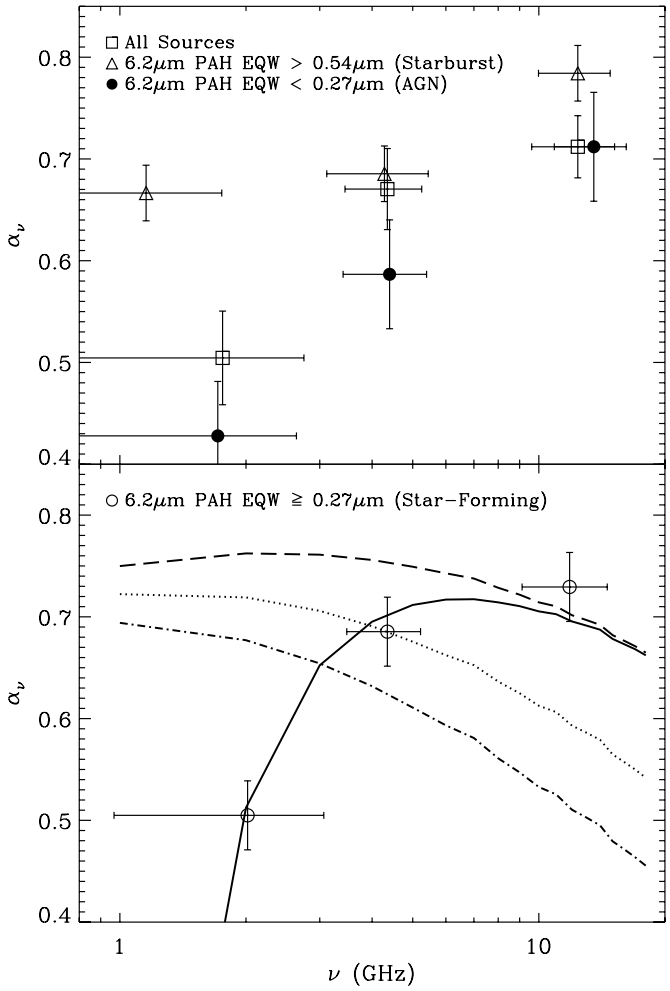

Figure 1. Median radio spectral indices calculated at three different frequency bins listed in Table 2. The horizontal error bars illustrate the standard deviation among the median frequencies per bin, while the vertical error bars illustrate the error on the median spectral index. In the top panel, sources are binned based on their 6.2 μm PAH EQWs, where starbursts (i.e., 6.2 μm PAH EQW > 0.54 μm) and AGNs (i.e., 6.2 μm PAH EQW < 0.27 μm) show statistically different average radio spectral indices in the low- and mid-frequency bins. As pointed out in Clemens et al. (2008), there is a clear trend of spectral flattening/steepening toward lower/higher frequencies among this sample of local IR-bright galaxies. In the bottom panel, only sources primarily powered by star formation (i.e., 6.2 μm PAH EQW $\geqslant$ 0.27 μm) are considered. Overplotted are expected spectral indices for star-forming galaxies having a non-thermal spectral index of $\alpha \approx 0.83$ and 1.4 GHz thermal fractions of $f_{\rm T}^{1.4\,{\rm GHz}} \approx 5\%$ (dashed line), 10% (dotted line), and 15% (dot-dashed line; see Figure 2). The solid line uses the expectation for the model with a 1.4 GHz thermal fraction of 5%, except it sets the free–free optical depth to unity at 1 GHz. This model seems to do a reasonable job fitting through the data points among the sample of star-formation-dominated sources.

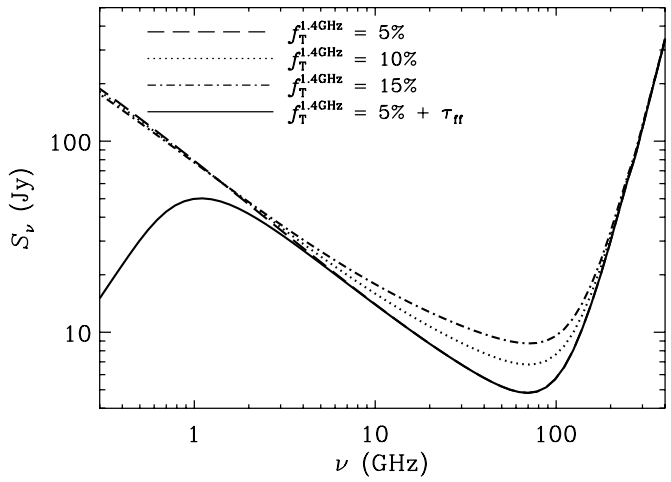

Figure 2. Model radio-to-IR galaxy spectra used for the comparison in Figure 1. The IR (8–1000 μm) flux is set to $F_{\rm IR} = 10^{-9}$ W m^{-2}, and it is assumed that the source follows the FIR/radio correlation. The radio spectra are constructed following the prescription given in Murphy (2009), resulting in a non-thermal spectral index of $\approx$0.83 with 1.4 GHz thermal radio fractions of $f_{\rm T}^{1.4\,{\rm GHz}} \approx 5\%$ (dashed line), 10% (dotted line), and 15% (dot-dashed line). The solid line is the same as the 5% thermal fraction at 1.4 GHz model, except that the free–free optical depth becomes unity at 1 GHz.

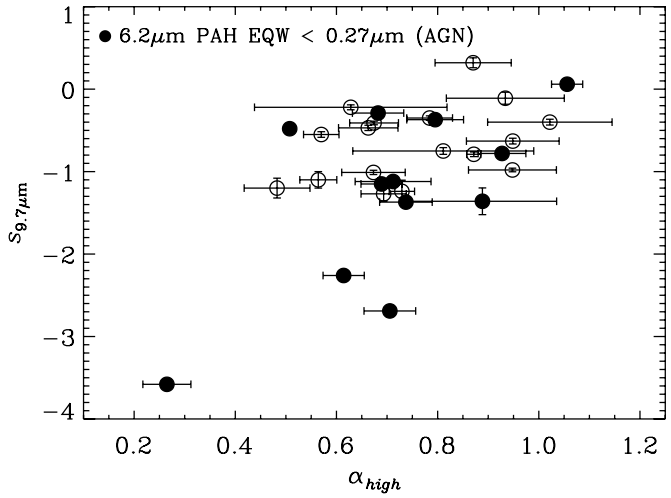

Figure 3. Strength of the 9.7 μm silicate feature plotted against the high-frequency radio spectral index (see Table 2). Sources categorized as being AGN-dominated by their low 6.2 μm PAH EQW are identified (filled circles). Unlike the radio spectral indices measured between 1.4 and 8.4 GHz (Murphy et al. 2013), there does not appear to be any correlation between the silicate strength and the high-frequency radio spectral indices, suggesting that the steep spectral indices at these frequencies may not be associated with the compactness of the starburst.

frequencies among this sample of local, merger-driven starburst galaxies, which is clearly discrepant from the expectations of typical radio spectra for star-forming galaxies. However, by taking the model having a 1.4 GHz thermal fraction of 5%, modified by free–free absorption where the free–free optical depth is $\tau_{\rm ff} = (\nu/\nu_{\rm b})^{-2.1}$ and becomes unity at $\nu_{\rm b} = 1$ GHz, the model largely fits the observed trend (solid line).

3.2. The High-frequency Indices Compared to the Compactness of the Sources

Recently, it has been shown that the flattening of the radio spectrum measured between 1.4 and 8.4 GHz (i.e., essentially the spectral index in the mid-frequency bin presented here) among this sample of local IR-bright starbursts increases with increasing 9.7 μm silicate optical depth, 8.44 GHz brightness temperature, and decreasing size of the radio source even after removing potential AGNs (Murphy et al. 2013), supporting the idea that compact starbursts show spectral flattening as the result of increased free–free absorption (Condon et al. 1991). In Figure 3 the strength of the 9.7 μm silicate feature is plotted against the high-frequency radio spectral index, indicating the absence of any such trend. Even after removing sources identified as harboring AGNs due to their small 6.2 μm PAH EQW, a trend is still not found. This indicates that the compactness of the starburst likely does not affect the steepness of the high-frequency radio spectrum.

3.3. The Radio Spectral Indices as a Function of Merger Stage

As already shown by Condon et al. (1991), there is a general trend among this sample of local starbursts in which more compact (i.e., higher surface brightness) sources tend to have flatter radio spectral indices, consistent with compact sources becoming optically thick at low (i.e., $\nu \lesssim 5$ GHz) radio frequencies. Another way one can illustrate this is by plotting the radio spectral index as a function of merger stage, which is done for the low-, mid-, and high-frequency radio spectral indices in Figure 4. The top, middle, and bottom panels plot radio spectral indices at frequencies of ∼2, 4, and 12 GHz, respectively, against merger stage. The horizontal lines in each panel correspond to the expected spectral index at that frequency given the model radio spectra shown in Figure 2. Only two models are shown: a normal star-forming galaxy having a 1.4 GHz thermal fraction of 10% and a star-forming galaxy with an original 1.4 GHz thermal fraction of 5% except that the free–free optical depth becomes unity at 1 GHz.

In the top and middle panels, it seems that the flattest spectrum sources falling below what is expected for a normal star-forming galaxy, as indicated by the dotted line, are only found in ongoing and post-mergers with strongly disturbed morphologies. The only outlier appears to be the non-merger IRAS F10173+0828, which has a flat spectrum at all frequency bins and hosts an OH megamaser (Mirabel & Sanders 1987) along with a highly compact radio core (Lonsdale et al. 1993). This finding is robust even after removal of potential AGNs as indicated by low 6.2 μm PAH EQWs. However, this trend does not persist when the high-frequency spectral indices, measured at ∼12 GHz, are plotted against merger sequence in the bottom panel. After removing potential AGNs, the steepest spectrum sources, lying well above what is expected for a normal star-forming galaxy as indicated by the dotted line, are only found among those sources categorized as ongoing mergers in which galaxy nuclei are distinct, but share a common envelope and/or exhibit tidal tails as observed in their stellar light. In contrast, pre- and post-stage mergers do not seem to exhibit such steep spectral indices. Thus, the low-, mid-, and high-frequency spectral indices each appear to be sensitive to the exact stage of the merger.

3.4. FIR-to-Radio Ratios as a Function of Merger Stage

In Figure 4 it has been shown that sources having the steepest spectra appear to be associated with systems classified as ongoing mergers in which the progenitors are separable and share a common envelope or display strong tidal features. To determine whether merger stage affects the total radio continuum emission, rather than just the spectral index, the differences between the nominal and observed logarithmic $F_{\rm FIR}$/radio ratios at 1.4 and 8.4 GHz are plotted in the top and bottom panels of Figure 5, respectively, against merger stage. The difference between the nominal and observed $F_{\rm FIR}$/radio ratios is defined as

$$\delta q_\nu = q_{0,\nu} - q_\nu, \quad (3)$$

such that a positive value indicates excess radio emission per unit FIR emission, and $q_{0,\nu}$ is the nominal $F_{\rm FIR}$/radio ratio for local star-forming systems. Under the assumption that the FIR emission is a good measure for the total star formation rate in each system, a large value of δq_ν indicates excess radio emission per unit star formation rate. At 1.4 GHz, $q_{0,1.4\,\rm GHz} \approx 2.34$ dex with a scatter of 0.26 dex among ∼1800 galaxies spanning nearly five orders of magnitude in luminosity (e.g., Yun et al.

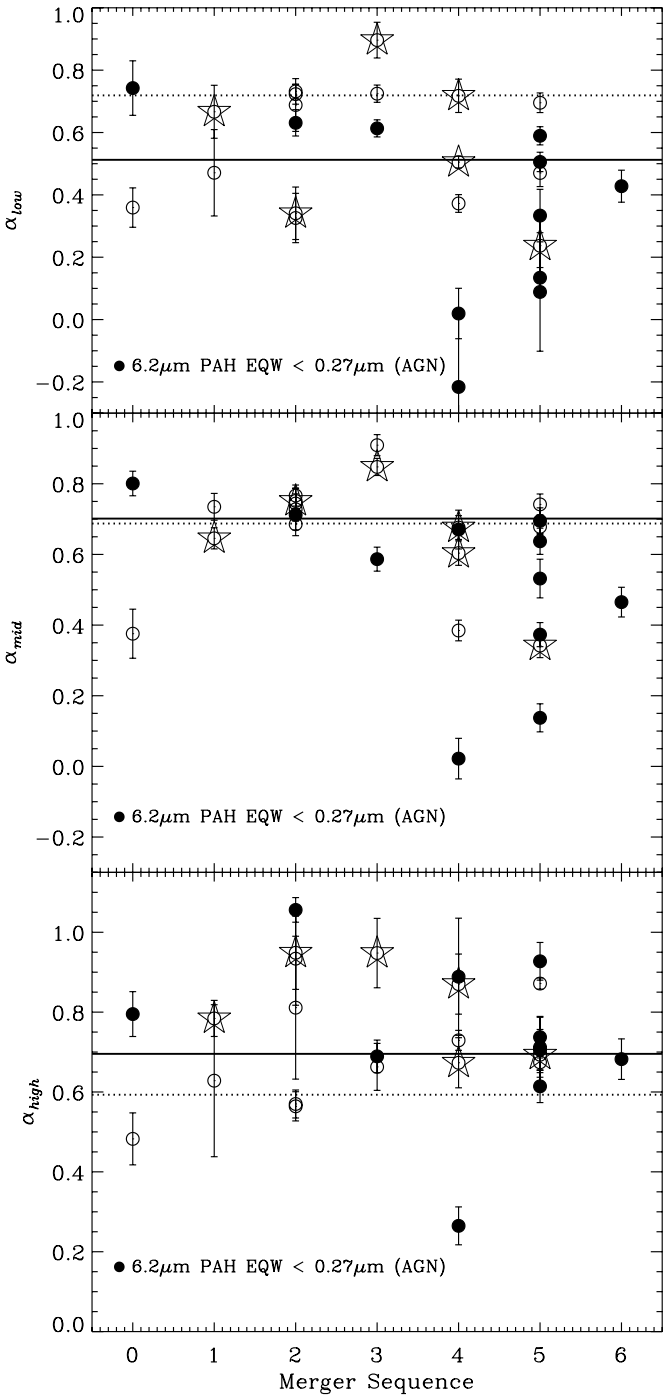

Figure 4. Low-, mid-, and high-frequency radio spectral indices (see Table 2), plotted against merger stage (see Section 2) in the top, middle, and bottom panels, respectively. The merger classification integers increase from isolated to post-merger systems. Sources categorized as being AGN-dominated by their low 6.2 μm PAH EQW are identified in each panel (filled circles). Those systems which are shown in Figure 6 are marked with a star. The horizontal lines in each panel correspond to the expected spectral index at that frequency given the model radio spectra shown in Figure 2. Only two models are shown; a normal star-forming galaxy having a 1.4 GHz thermal fraction of 10% (dotted line), and a star-forming galaxy with an original 1.4 GHz thermal fraction of 5% before being modified by free–free absorption in which the free–free optical depth becomes unity at 1 GHz (solid line). Low- and mid-frequency radio spectral indices are found to be flat only for those sources classified as ongoing mergers with strongly disturbed morphologies and post-stage mergers. For the high-frequency radio spectral indices, the steepest values are found for systems classified as ongoing mergers with progenitors sharing a common envelope after removing AGNs.

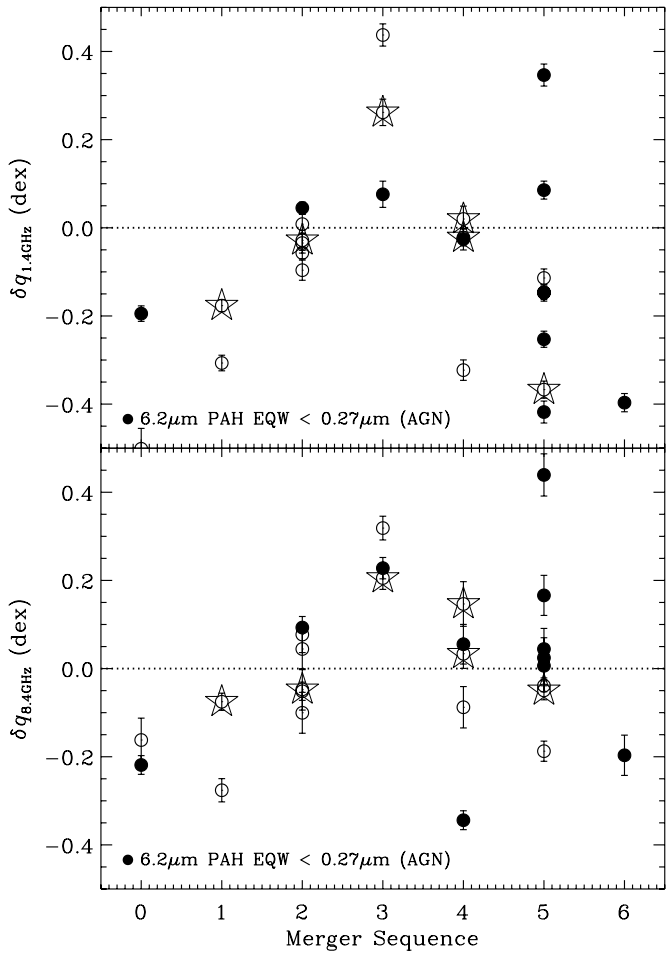

Figure 5. Top: the difference between the observed and nominal logarithmic F_{FIR}-to-1.4 GHz flux density ratios (see Section 3.4), such that positive numbers indicate an excess of 1.4 GHz radio continuum emission per unit star formation rate, assuming that the star formation rate is linearly proportional to the FIR emission, plotted against merger stage (see Section 2; numbers increase from isolated to post-merger systems). Bottom: the same as the top panel, except using the difference between the observed and nominal F_{FIR}-to-8.4 GHz flux density ratios that, unlike the 1.4 GHz data, are less affected by spectral flattening due to the increased free–free optical depth in the most compact starbursts. Sources categorized as being AGN-dominated by their low 6.2 μm PAH EQW are identified in each panel (filled circles). Those systems that are shown in Figure 6 are marked with a star. In both panels, there seems to be a clear amount of excess radio emission relative to FIR emission among systems classified as ongoing mergers with progenitors sharing a common envelope. This distinction appears even more pronounced when potential AGNs are removed.

2001), among other properties (e.g., Hubble type, FIR color, and F_{FIR}/optical ratio). Assuming a typical radio spectrum, with a spectral index of $\alpha \approx 0.8$ (Condon 1992), this translates into a nominal F_{FIR}-to-8.4 GHz flux density ratio of $q_{0,8.4\,\mathrm{GHz}} \approx 2.94$ dex.

In the top panel of Figure 5, it can be shown that galaxies having the largest 1.4 GHz excesses appear to be ongoing mergers that share a common envelope before and after removal of potential AGNs. However, there is a good deal of scatter in this figure, and there are a number of sources for which significant excesses of FIR emission are observed relative to the measured 1.4 GHz flux densities. Since the $q_{1.4\,\mathrm{GHz}}$ ratios are clearly affected by free–free absorption at low frequencies in the most compact starbursts (Condon et al. 1991), it may be better to see if such a trend persists using emission at a higher frequency, where free–free absorption is considered to be largely negligible, such as 8.4 GHz. This is shown in the bottom panel of Figure 5, where $\delta q_{8.4\,\mathrm{GHz}}$ is plotted against merger stage and the exact same behavior is found, albeit with a much smaller dispersion per merger sequence bin. Excluding potential AGNs, there appears to be a trend in which sources classified as ongoing mergers that share a common envelope have excess radio emission per unit star formation rate relative to both early and post-stage mergers, which exhibit nominal F_{FIR}/radio ratios. Thus, similar to radio spectral indices, the FIR-to-radio ratios appear to be sensitive to merger stage.

4. DISCUSSION

As previously stated, a number of physical scenarios to explain the steep radio spectral indices among this sample of local starburst galaxies have been proposed in the literature, particularly by the original study of Clemens et al. (2008). While simple arguments to produce steep spectra via increased synchrotron and inverse Compton losses appear to fall short, given that the most compact starbursts are not the sources that exhibit the steepest spectra, an alternative explanation is proposed. It has been know for some time that, when caught in the act, merging systems can create bridges of synchrotron emission that stretch between the progenitor galaxies, whose brightness contours resemble stretching strands of "taffy" (Condon et al. 1993). The two most well-known cases of "taffy" galaxies are the face-on colliding systems UGC 12914/5 (Condon et al. 1993) and UGC 813/6 (Condon et al. 2002).

The spaces between the spiral galaxy pairs UGC 12915/5 and UGC 813/6 are filled with synchrotron emission, implying that they must contain both relativistic electrons and magnetic fields. The magnetic field of the bridge is presumably stripped from the merging spiral galaxy disks as they interpenetrated during a recent collision; however, there is some debate as to whether the relativistic electrons in the bridge have escaped the merging spirals, as originally suggested by Condon et al. (1993), or are rather a new population of relativistic electrons that have been diffusively accelerated in a shock associated with a gas dynamical interaction during the merger (Lisenfeld & Völk 2010). As discussed below, if such a scenario is also responsible for the properties of the starbursting mergers investigated here, the latter explanation appears more appealing.

Other prominent features of the "taffy" systems include (1) an exceptionally steep spectrum located at the center of the radio bridges (i.e., $\alpha \approx 1.3$, which is roughly $\Delta\alpha = 0.5$ steeper than the spectral indices of the galaxy disks); (2) a ratio of F_{FIR}/radio emission for the entire system that is significantly lower than that of normal star-forming galaxies, but typical for the individual spiral galaxy disks; (3) a significant fraction of H I stripped by the collisions that resides between the spiral disks; (4) a significant amount of molecular gas in the bridge (Braine et al. 2003) whose physical conditions are comparable to those in the diffuse clouds of the Galaxy (Zhu et al. 2007); (5) a small amount of warm (i.e., 5–17 μm; Jarrett et al. 1999) and cold (i.e., 450 and 850 μm; Zhu et al. 2007) dust located in the bridge, indicating a low amount of ongoing star formation; (6) rotational lines of H_2 emission that dominate the mid-IR spectrum and appear strongest near the center of the bridge (Peterson et al. 2012).

4.1. "Taffy"-like Starbursts

Among the merging starbursts investigated here, those having the steepest high-frequency ($\nu \sim 12$ GHz) radio spectra and

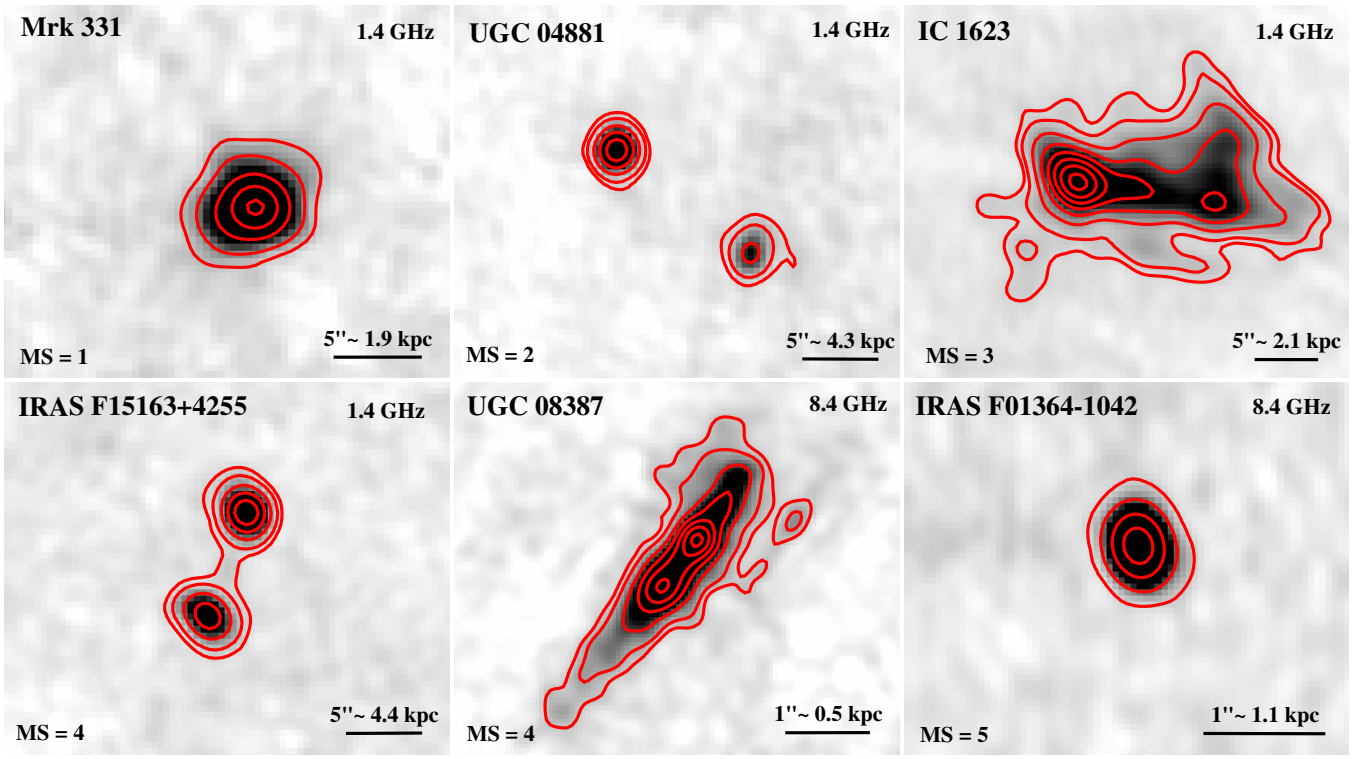

Figure 6. Radio continuum maps and contours for six non-AGN systems, chosen to span the range of merger stages classified through *HST* imaging, are displayed (merger stage classifications are given in the lower left corner of each panel). For Mrk 331, UGC 04881, IC 1623, and IRAS F15163+4255, 1.4 GHz maps from Condon et al. (1990) are shown, all having resolutions of 1.″5 except for IC 1623 (2.″1). However, for the more compact sources UGC 08387 and IRAS F01364−1042, the higher resolution (0.″25) 8.4 GHz maps from Condon et al. (1991) are shown. The contour levels start at three times the rms noise of each map and are shown using a square-root scaling. For the pre-merger, Mrk 331, its companion galaxy is not shown in the panel, as it is ≈2′ away.

(A color version of this figure is available in the online journal.)

significant excesses of radio emission relative to their observed FIR emission appear to be galaxies in an ongoing merger and either share a common stellar envelope or have significant tails. Both of these radio characteristics are also found in "taffy" systems, whose steep spectra and excess radio emission per unit star formation rate arise from the radio continuum emission in the bridge connecting the merging galaxies. Given that simple physical arguments based on the escape and radiative cooling times of CR electrons to explain these properties among local compact starbursts fail, a "taffy"-like merger scenario appears to be an appealing way to explain the low $F_{\rm FIR}$/radio ratios and steep high-frequency spectra.

In Figure 6, radio continuum maps are shown for six galaxies that largely span the full merging sequence and do not appear to harbor buried AGNs based on their measured 6.2 μm PAH EQWs. Each system has been highlighted as a star in Figures 4 and 5. Mrk 331 is a pre-merger, exhibiting a symmetric 1.4 GHz radio continuum morphology, as well as a typical radio spectrum and $F_{\rm FIR}$/radio ratio. UGC 04881 is characterized as an ongoing merger with separable progenitor galaxies. IC 1623 is optically classified as an ongoing merger whose progenitors share a common envelope, which is consistent with its 1.4 and 8.4 GHz radio morphologies. It has a high-frequency radio spectral index of ≈0.95 and a factor of 1.6 excess radio emission relative to what is expected given the FIR/radio correlation. The excess radio emission appears easily explained by summing the diffuse synchrotron emission that is not associated with the colliding star-forming galaxy disks. IRAS F15163+4255 is classified (by the *HST* data) as an ongoing merger with two nuclei and a prominent tidal tail. This source has very weak 1.4 and 8.4 GHz radio continuum emission that appears to form a bridge between the two progenitor galaxies, keeping it right on the FIR/radio correlation. This source also exhibits a somewhat steep high-frequency radio spectral index of ≈0.84. Like IRAS F15163+4255, UGC 08387 is also classified as an ongoing merger harboring two nuclei and a prominent tidal tail. Given that the progenitor galaxies are not separated by a large angular extent, the high (0.″25) 8.4 GHz radio continuum map of Condon et al. (1991) is necessary to resolve both components. Similar to IC 1623, the 8.4 GHz morphology is consistent with its optical merger classification, as there are tidal tails of synchrotron emission. UGC 08387 has a high-frequency radio spectral index of ≈0.70 and 40% excess radio emission at 8.4 GHz than expected given its FIR flux. Finally, the post-stage, ultra-compact merger IRAS F01364+1042 is shown, also requiring the use of the high-resolution 8.4 GHz radio map, in which their appears to be a single source having seemingly undisturbed radio continuum contours. This system has an extremely flat low- and mid-frequency radio spectral index, presumably due to free–free absorption occurring in the compact starbursts, but a rather normal high-frequency spectral index. Consequently, its $q_{1.4\,\rm GHz}$ value is significantly larger than average, unlike its rather typical $q_{8.4\,\rm GHz}$ value.

Focusing in on IC 1623, 1.4 to 8.4 GHz (4.″7 resolution) spectral index contours are overlaid on an *I*-band (F814W) *HST*/ACS image in Figure 7. The radio spectral indices are found to be rather typical relative to normal star-forming galaxies for both merging galaxy disks (i.e., $\alpha_{1.4\,\rm GHz}^{8.4\,\rm GHz} \sim 0.7$). The eastern galaxy disk hosts the most deeply embedded star formation, and the radio spectral index clearly flattens right on the peak of the starburst. Similar to the "taffy" systems, the radio spectral index is found to steepen significantly along the radio continuum

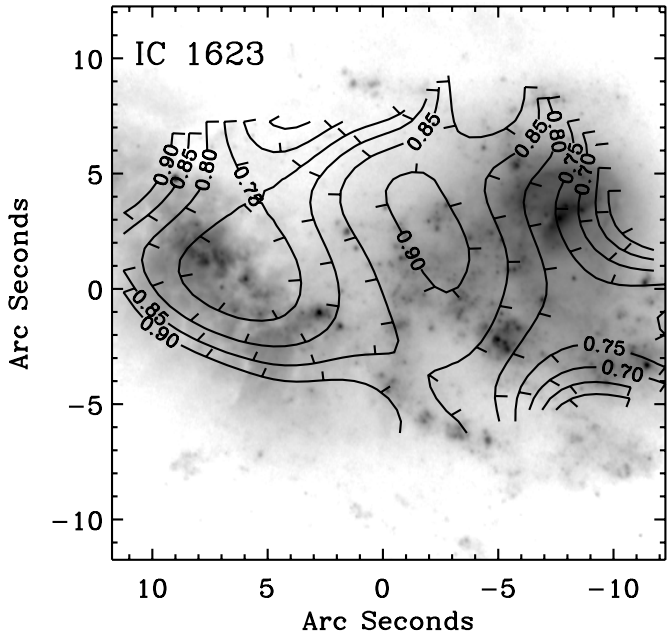

Figure 7. Spectral index (1.4 to 8.4 GHz) contours overlaid on an *HST*/ACS image of IC 1623 taken with the F184W (*I*-band) filter (Kim et al. 2013). The resolution of the spectral index contours is 4.″7, set by the natural-weighted 8.4 GHz image from Clemens et al. (2008). The radio spectral index is flattest on the IR-bright starburst core to the east ($\alpha_{1.4\,\mathrm{GHz}}^{8.4\,\mathrm{GHz}} \approx 0.7$), which is still typical for normal star-forming galaxies. The spectral index along the much less dust-obscured western galaxy disk is also normal, being $\alpha_{1.4\,\mathrm{GHz}}^{8.4\,\mathrm{GHz}} \approx 0.75$. However, similar to the "taffy" galaxies, the radio spectrum steepens significantly along the radio continuum bridge connecting the galaxy pair, peaking at $\alpha_{1.4\,\mathrm{GHz}}^{8.4\,\mathrm{GHz}} \approx 0.92$ at the midpoint between the interacting disks.

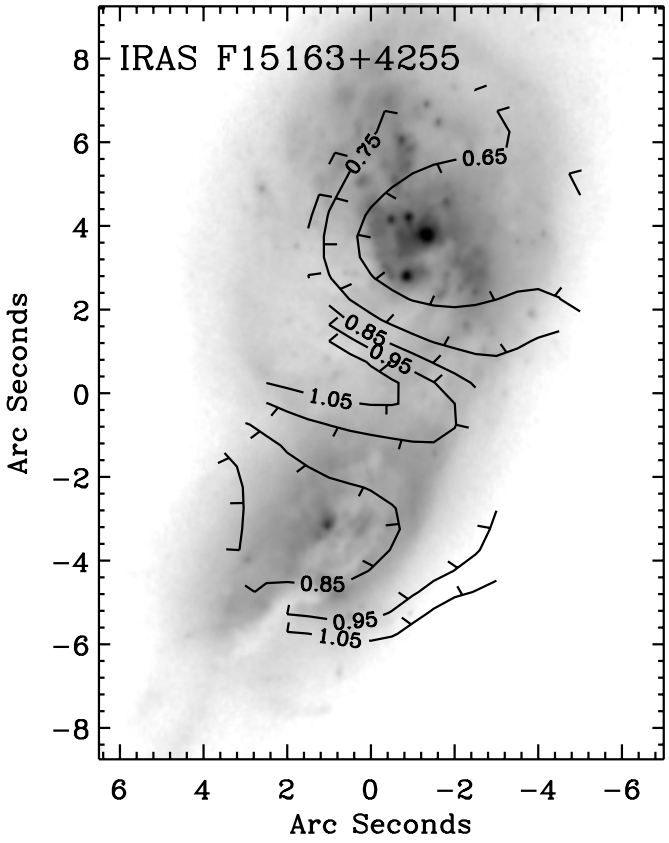

Figure 8. Spectral index (1.4 to 8.4 GHz) contours overlaid on an *HST*/ACS image of IRAS F15163+4255 taken with the F184W (*I*-band) filter (Kim et al. 2013). The resolution of the spectral index contours is 3.″1, set by the natural-weighted 8.4 GHz image from Clemens et al. (2008). The radio spectral index of the southern galaxy is $\alpha_{1.4\,\mathrm{GHz}}^{8.4\,\mathrm{GHz}} \approx 0.8$, which is still typical for normal star-forming galaxies. The spectral index of the brighter northern galaxy is significantly flatter, being $\alpha_{1.4\,\mathrm{GHz}}^{8.4\,\mathrm{GHz}} \approx 0.6$. Similar to the "taffy" galaxies, the radio spectrum steepens significantly along the (in this case very weak) radio continuum bridge connecting the galaxy pair, peaking at $\alpha_{1.4\,\mathrm{GHz}}^{8.4\,\mathrm{GHz}} \approx 1.1$ at the midpoint between the interacting disks.

bridge connecting the galaxy pair, peaking roughly at the midpoint between the two galaxy disks with $\alpha_{1.4\,\mathrm{GHz}}^{8.4\,\mathrm{GHz}} \approx 0.92$. Furthermore, like the "taffy" systems, high-resolution ^{12}CO observations show a significant amount of molecular gas located in the overlap regions connecting the two galaxy nuclei (Yun et al. 1994; Iono et al. 2004), thus providing material for the galactic magnetic fields to be anchored as they stretch during the merger process. A similar situation is observed by plotting the 1.4 to 8.4 GHz (3.″1 resolution) spectral index contours on the *I*-band (F814W) *HST*/ACS image of IRAS F15163+4255 in Figure 8. While the northern and southern galaxy nuclei appear to have significantly different spectral indices, peaking around $\alpha_{1.4\,\mathrm{GHz}}^{8.4\,\mathrm{GHz}} \approx 0.6$ and $\alpha_{1.4\,\mathrm{GHz}}^{8.4\,\mathrm{GHz}} \approx 0.8$, respectively, there is a strong steepening of the indices toward the emission connecting the two galaxy nuclei peaking at $\alpha_{1.4\,\mathrm{GHz}}^{8.4\,\mathrm{GHz}} \approx 1.1$ at the midpoint between the interacting disks.

Explaining the steep radio spectral indices and lower than average F_{FIR}/radio ratios as the result of ongoing mergers seems to be fairly well supported by the data. To date, it has been hard to explain the steep high-frequency spectra in this sample of starbursts given that the rapid ($\sim 10^4$ yr) synchrotron and inverse Compton cooling times render diffusion and escape losses to be negligible and thus cannot work to steepen the spectra. In fact, escape as an explanation is in disagreement with the data, given that the loss of CR electrons would effectively lower the total synchrotron power, whereas galaxies with steep high-frequency spectral indices can have low F_{FIR}/radio ratios. Creating a magnetized medium through the dynamical interaction of the merging galaxy pairs, similar to that of the "taffy" systems, provides a location where the CR electrons can radiatively cool without the continuous injection and acceleration of new particles.

Given the rapid cooling times due to radiative losses in the compact starbursts embedded in the merging disks, it seems unlikely that the relativistic electrons associated with synchrotron bridges and/or tidal tails were injected and accelerated in the starburst itself and have propagated to such distances. As an example, the distance to the midpoint between the two 1.4 GHz "hot spots" in the merging disks of IC 1623 is $\approx 5''$, which projects to a linear distance of $\approx$2 kpc at a distance of 85.5 kpc. This distance is actually smaller than the $\approx 15''$ (6 kpc) separation between the two galaxy nuclei. Following the description for propagation and physical processes responsible for CR electron energy losses given in Murphy (2009), it can be shown that the time for 1.4 GHz emitting electrons to reach this midpoint is significantly longer than their radiative lifetime. Assuming random walk diffusion, characterized by an energy-dependent diffusion coefficient, the propagation time is $\sim 2.6 \times 10^7$ yr. The radiative lifetime for CR electrons emitted within a 2.″5 radius of the western galaxy, which likely includes the bulk 1.4 GHz emission associated with star formation in that disk, is $\sim 2.9 \times 10^5$ yr, nearly two orders of magnitude shorter.

Additionally, the time that the merger is expected to spend in either of these classifications is no more than a few times $\sim 10^7$ yr (Haan et al. 2011), which is roughly an order of magnitude longer than the synchrotron cooling times of CR electrons that

may populate a bridge, assuming that the magnetic field stays in equipartition with the disk it is being pulled out of, and that the radiation field and ISM density lead to negligible inverse Compton and bremsstrahlung cooling, respectively. Thus, it appears more likely that charged particles in such regions have been diffusively accelerated via shocks associated with the available mechanical energy of the merger (e.g., Lisenfeld & Völk 2010). The speed of the galaxy collisions is a few $\sim$100 km s^{-1} (e.g., G. Privon et al. 2014, in preparation), and therefore super-Alfvénic for typical ISM Alfvén speeds a few $\sim$10 km s^{-1}. The Alfvénic Mach number is much larger than unity, at the order $M_{\rm A}^2 \sim \mathcal{O}(100) \gg 1$, allowing for shocks that can diffusively accelerate CR particles. This is similar to the Alfvénic Mach numbers within the Sedov–Taylor expansion phase of SNRs.

This explanation for diffusive acceleration via shocks associated with the merger is additionally supported by integral field spectroscopic observations of IR-bright mergers. For the case of IC 1623, Rich et al. (2011) have shown that optical emission line diagnostic ratios indicate the presence of widespread shock excitation induced by ongoing merger activity. The energy associated with the shocks in the interacting regions between the two galaxy disks is estimated to be $\sim 4 \times 10^{42}$ erg s^{-1} based on the amount of Hα line emission having widths $\gtrsim$100 km s^{-1} in the interacting region (i.e., $80 \times L_{\rm H\alpha}$, where $L_{\rm H\alpha} \sim 5 \times 10^{40}$ erg s^{-1}; Rich et al. 2010, 2011). This value is nearly a factor of $\sim 1.5 \times 10^3$ times larger than the total 8.4 GHz luminosity of the source ($\nu L_{8.4\,\rm GHz} \sim 3 \times 10^{39}$ erg s^{-1}), suggesting that, for a proton-to-electron ratio of $\sim$100 in this GeV energy range, $\sim$4% of the total mechanical luminosity from the shock needs to go into accelerating CRs to explain a factor of $\sim$2 extra radio emission. This is much less than the typical 10%–30% efficiency of particle acceleration in SNRs (e.g., Berezhko & Völk 1997; Kang & Jones 2005; Caprioli et al. 2010).

4.2. The Case for a Steeper Injection Spectrum in Dense Starbursts

While it is argued here that the most likely explanation for both the steep high-frequency radio spectra and "excess" radio emission in this sample of local starbursts arises from synchrotron bridges and tails associated with the stage of the merger, another explanation that has not been currently explored is a systematic change (steepening) in the injection spectrum in this sample of starbursts. Naively, such a scenario does not seem that implausible given the ISM conditions in dense starbursts.

The efficiency in which CRs are accelerated in SNRs plays a significant role in determining the synchrotron emissivity from galaxies. One could imagine a scenario in which the adiabatic phase of SNe is halted as it expands into the ambient medium, thus reducing the amount of energy lost to adiabatic expansion and leaving "extra" energy that could be used in the acceleration of CRs, thereby increasing the total synchrotron emission per unit star formation rate relative to normal galaxies. For example, the modeling of Dorfi (1991, 2000) shows that the total acceleration efficiency for CRs increases from $\sim 0.15 E_{\rm SN}$ to $\sim 0.25 E_{\rm SN}$, where $E_{\rm SN} = 10^{51}$ erg is the total explosion energy of the SNe, when the external ISM density is increased from $\sim$1 cm^{-3} to $\sim$10 cm^{-3}. Additionally, an increase in the injection efficiency can work to steepen the CR injection spectrum (Caprioli 2012). The ISM densities of starbursts are typically much larger (e.g., $n_{\rm ISM} \sim 10^4$ cm^{-3}), thus the evolution of SNRs will likely be different and may work to increase the synchrotron emissivity in such galaxies through an increased efficiency in particle acceleration, as well as result in steeper radio spectra due to a steeper initial injection spectrum.

However, given that the densest starbursts, which exhibit the flattest low- and mid-frequency spectral indices, are associated with late-/post-stage mergers and also have typical high-frequency radio spectral indices as well as normal $F_{\rm FIR}$/radio flux density ratios, this explanation seems less likely. This additionally suggests that the excess radio emission in starbursts as a result of increased secondary electrons may not be a likely explanation (e.g., Murphy 2009; Lacki et al. 2010), since the densest starbursts (i.e., post mergers) provide the environment for which secondary production should be the most efficient. For example, in a dense starburst, having a much larger ISM density, the cross-section for collisions between CR nuclei and the interstellar gas is increased, thus increasing the number of $e^{\pm}$'s for a fixed primary nuclei/electron ratio, which may actually dominate the diffuse synchrotron emission. Yet, the densest, post-merger starbursts do not show evidence for excess radio emission per unit star formation rate like those systems in which the progenitors are still clearly separated and exhibit a non-negligible amount of diffuse radio emission in features such as bridges and tails.

4.3. An Explanation for Low FIR/Radio Ratios in High-z SMGs?

A significant fraction of submillimeter galaxies (SMGs) detected at redshifts between $2 \lesssim z \lesssim 4$ similarly show excess (i.e., a factor of $\gtrsim$3) radio emission relative to their total FIR emission and a nominal $F_{\rm FIR}$/radio ratio (e.g., Kovács et al. 2006; Valiante et al. 2007; Capak et al. 2008; Murphy et al. 2009; Daddi et al. 2009b, 2009a; Coppin et al. 2009; Knudsen et al. 2010; Smolčić et al. 2011), although it is worth pointing out that this is not true for all samples of SMGs at these redshifts (e.g., Chapman et al. 2010). AGNs provide a likely explanation for the excess radio emission in such sources given that a number are detected in hard (2.0–8.0 keV) X-rays (Alexander et al. 2005); however, it is possible that those sources without evidence for AGNs may exhibit excess radio emission associated with being involved in an ongoing merger.

At such cosmological distances, it is currently unclear what fraction of SMGs are major mergers rather than isolated disks, but the morphologies for a number of resolved sources seem to suggest major mergers that are driving intense bursts of star formation (e.g., Chapman et al. 2003; Hodge et al. 2013). With the Atacama Large Millimeter/submillimeter Array (ALMA) now online, resolving these dusty starbursts into individual components is becoming easier (e.g., Hezaveh et al. 2013; Hodge et al. 2013). For instance, the lensed star-forming galaxy SPT-S 053816-5030.8, at a redshift of $z = 2.783$, has a radio spectrum that appears to flatten ($\alpha \approx 0.18$) toward low frequencies, while having a rather steep ($\alpha \approx 0.76$) spectrum at high frequencies (Aravena et al. 2013), similar to what is seen among the local compact starbursts investigated here. While the estimated (rest-frame) $q_{1.4\,\rm GHz}$ value for this source is slightly larger than the local average value, consistent with expectations given the spectral flattening at lower frequencies assuming optically thick free–free emission, the $q_{8.3\,\rm GHz}$ value is $\approx$0.36 dex smaller than the local average value, implying excess radio emissions per unit star formation rate.

New imaging at 350 GHz using ALMA along with lens modeling (Hezaveh et al. 2013) suggests that this SMG is in fact composed of two galaxies, one of which is a compact source that dominates the FIR emission. Both the radio continuum

properties and 350 GHz morphology suggest that the source is consistent with being powered by merger-driven star formation as observed in local (U)LIRGs. Thus, at least for this SMG, excess non-thermal radio emission associated with the merger may provide a natural explanation for its steep radio spectral index at high frequencies and presumably excess radio emission per unit star formation rate relative to normal star-forming galaxies rather than requiring the need to invoke cosmic conspiracies (e.g., Lacki & Thompson 2010). Having better multi-frequency radio data for a large number of these high-redshift SMGs, to see if their spectra are also steep at high frequencies, may help to explain exactly why this population of starbursting galaxies appear to have significantly more radio emission per unit star formation rate than expected.

5. CONCLUSIONS

An examination of the radio continuum properties for a sample of local IR-bright starbursts has been investigated against their merger classification. This was done to shed light on the curious nature of the radio spectra among such sources, specifically those having steeper than expected radio spectra observed at frequencies ∼12 GHz as pointed out by Clemens et al. (2008). The main conclusions from this investigation can be summarized as follows.

1. Sources categorized as starbursts and AGNs via their 6.2 μm PAH EQWs have similar high-frequency ($\nu \sim$ 12 GHz) radio spectral indices, suggesting that the steep spectra among some sources at these frequencies are not the result of radio emission associated with an AGN.
2. Sources having the steepest radio spectral indices at ∼12 GHz, while also appearing to be powered primarily by star formation as indicated by their 6.2 μm PAH EQWs, are classified as ongoing mergers in which the progenitors are still separated and either share a common envelope or show significant tidal tails in their stellar light. Similarly, these same galaxies also exhibit excess radio emission relative to what is expected given their observed FIR emission and the tight FIR/radio correlation, suggesting that there is excess radio emission not associated with ongoing star formation activity. The combination of these observations leads to a picture in which the steep high-frequency radio spectral indices and excess radio emission arises from radio continuum bridges and tidal tails in which a new population of relativistic electrons have been accelerated and can radiatively cool, producing a steep spectrum. Such a scenario is consistent with high-resolution radio morphologies of the sources as a function of merger stage, as well as the radio spectral index map for the merging galaxy pairs IC 1623 and IRAS F15163+4255.
3. Among all sources whose energetics are thought to be dominated by star formation given their 6.2 μm PAH EQWs, their average radio spectral indices at ∼2, 4, and 12 GHz appear to be fairly well fit by a model radio spectrum having a non-thermal radio spectral index of ≈0.83 and a 1.4 GHz thermal fraction of ≈5% (corresponding to ≈33% at 30 GHz) modified by free–free absorption where the free–free optical depth becomes unity at ≈1 GHz.

I thank the anonymous referee for useful comments that helped to significantly improve the content and presentation of this paper. I also thank S. Stierwalt, S. Haan, J. A. Rich, G. C. Privon, L. Armus, L. Barcos, A.K. Leroy, and P.A. Appleton for useful discussions, M. Clemens for providing reduced X-band maps, and D.-C. Kim and A.S. Evans for providing their reduced *HST* images. I am also grateful to J.J. Condon for giving the paper a careful reading and providing useful comments. Finally, I acknowledge the hospitality of the Aspen Center for Physics, which is supported by the National Science Foundation Grant No. PHY-1066293. The National Radio Astronomy Observatory is a facility of the National Science Foundation operated under cooperative agreement by Associated Universities, Inc. This work is based in part on observations made with the *Spitzer Space Telescope*, which is operated by the Jet Propulsion Laboratory, California Institute of Technology, under a contract with NASA. This research has made use of the NASA/IPAC Extragalactic Database (NED), which is operated by the Jet Propulsion Laboratory, California Institute of Technology, under contract with the National Aeronautics and Space Administration.

REFERENCES

Alexander, D. M., Bauer, F. E., Chapman, S. C., et al. 2005, ApJ, 632, 736
Aravena, M., Murphy, E. J., Aguirre, J. E., et al. 2013, MNRAS, 433, 498
Armus, L., Charmandaris, V., Bernard-Salas, J., et al. 2007, ApJ, 656, 148
Armus, L., Heckman, T., & Miley, G. 1987, AJ, 94, 831
Armus, L., Heckman, T. M., & Miley, G. K. 1988, ApJL, 326, L45
Armus, L., Heckman, T. M., & Miley, G. K. 1989, ApJ, 347, 727
Armus, L., Heckman, T. M., & Miley, G. K. 1990, ApJ, 364, 471
Armus, L., Mazzarella, J. M., Evans, A. S., et al. 2009, PASP, 121, 559
Berezhko, E. G., & Völk, H. J. 1997, APh, 7, 183
Braine, J., Davoust, E., Zhu, M., et al. 2003, A&A, 408, L13
Brandl, B. R., Bernard-Salas, J., Spoon, H. W. W., et al. 2006, ApJ, 653, 1129
Capak, P., Carilli, C. L., Lee, N., et al. 2008, ApJL, 681, L53
Caprioli, D. 2012, JCAP, 07, 038
Caprioli, D., Kang, H., Vladimirov, A. E., & Jones, T. W. 2010, MNRAS, 407, 1773
Caputi, K. I., Lagache, G., Yan, L., et al. 2007, ApJ, 660, 97
Chapman, S. C., Ivison, R. J., Roseboom, I. G., et al. 2010, MNRAS, 409, L13
Chapman, S. C., Windhorst, R., Odewahn, S., Yan, H., & Conselice, C. 2003, ApJ, 599, 92
Chary, R., & Elbaz, D. 2001, ApJ, 556, 562
Clemens, M. S., Scaife, A., Vega, O., & Bressan, A. 2010, MNRAS, 405, 887
Clemens, M. S., Vega, O., Bressan, A., et al. 2008, A&A, 477, 95
Condon, J. J. 1992, ARA&A, 30, 575
Condon, J. J., Helou, G., & Jarrett, T. H. 2002, AJ, 123, 1881
Condon, J. J., Helou, G., Sanders, D. B., & Soifer, B. T. 1990, ApJS, 73, 359
Condon, J. J., Helou, G., Sanders, D. B., & Soifer, B. T. 1993, AJ, 105, 1730
Condon, J. J., Huang, Z.-P., Yin, Q. F., & Thuan, T. X. 1991, ApJ, 378, 65
Coppin, K. E. K., Smail, I., Alexander, D. M., et al. 2009, MNRAS, 395, 1905
Daddi, E., Dannerbauer, H., Krips, M., et al. 2009a, ApJL, 695, L176
Daddi, E., Dannerbauer, H., Stern, D., et al. 2009b, ApJ, 694, 1517
de Jong, T., Klein, U., Wielebinski, R., & Wunderlich, E. 1985, A&A, 147, L6
Dorfi, E. A. 1991, A&A, 251, 597
Dorfi, E. A. 2000, Ap&SS, 272, 227
Genzel, R., Lutz, D., Sturm, E., et al. 1998, ApJ, 498, 579
Gregory, P. C., & Condon, J. J. 1991, ApJS, 75, 1011
Haan, S., Surace, J. A., Armus, L., et al. 2011, AJ, 141, 100
Helou, G., Soifer, B. T., & Rowan-Robinson, M. 1985, ApJL, 298, L7
Hezaveh, Y. D., Marrone, D. P., Fassnacht, C. D., et al. 2013, ApJ, 767, 132
Hodge, J. A., Karim, A., Smail, I., et al. 2013, ApJ, 768, 91
Houck, J. R., Roellig, T. L., van Cleve, J., et al. 2004, ApJS, 154, 18
Iono, D., Ho, P. T. P., Yun, M. S., et al. 2004, ApJL, 616, L63
Jarrett, T. H., Helou, G., Van Buren, D., Valjavec, E., & Condon, J. J. 1999, AJ, 118, 2132
Kang, H., & Jones, T. W. 2005, ApJ, 620, 44
Kim, D.-C., Evans, A. S., Vavilkin, T., et al. 2013, ApJ, 768, 102
Knudsen, K. K., Kneib, J.-P., Richard, J., Petitpas, G., & Egami, E. 2010, ApJ, 709, 210
Kovács, A., Chapman, S. C., Dowell, C. D., et al. 2006, ApJ, 650, 592
Lacki, B. C., & Thompson, T. A. 2010, ApJ, 717, 196
Lacki, B. C., Thompson, T. A., & Quataert, E. 2010, ApJ, 717, 1
Le Floc'h, E., Papovich, C., Dole, H., et al. 2005, ApJ, 632, 169
Leroy, A. K., Evans, A. S., Momjian, E., et al. 2011, ApJL, 739, L25
Lisenfeld, U., & Völk, H. J. 2010, A&A, 524, A27

Lisenfeld, U., Wilding, T. W., Pooley, G. G., & Alexander, P. 2004, MNRAS, 349, 1335
Lonsdale, C. J., Smith, H. J., & Lonsdale, C. J. 1993, ApJL, 405, L9
Magnelli, B., Popesso, P., Berta, S., et al. 2013, A&A, 553, A132
Mirabel, I. F., & Sanders, D. B. 1987, ApJ, 322, 688
Murphy, E. J. 2009, ApJ, 706, 482
Murphy, E. J., Bremseth, J., Mason, B. S., et al. 2012, ApJ, 761, 97
Murphy, E. J., Chary, R., Alexander, D. M., et al. 2009, ApJ, 698, 1380
Murphy, E. J., Chary, R.-R., Dickinson, M., et al. 2011a, ApJ, 732, 126
Murphy, E. J., Condon, J. J., Schinnerer, E., et al. 2011b, ApJ, 737, 67
Murphy, E. J., Stierwalt, S., Armus, L., Condon, J. J., & Evans, A. S. 2013, ApJ, 768, 2
Murphy, T. W., Jr., Armus, L., Matthews, K., et al. 1996, AJ, 111, 1025
Niklas, S., Klein, U., & Wielebinski, R. 1997, A&A, 322, 19
Peterson, B. W., Appleton, P. N., Helou, G., et al. 2012, ApJ, 751, 11
Rich, J. A., Dopita, M. A., Kewley, L. J., & Rupke, D. S. N. 2010, ApJ, 721, 505
Rich, J. A., Kewley, L. J., & Dopita, M. A. 2011, ApJ, 734, 87
Sanders, D. B., Mazzarella, J. M., Kim, D.-C., Surace, J. A., & Soifer, B. T. 2003, AJ, 126, 1607
Sanders, D. B., Soifer, B. T., Elias, J. H., Neugebauer, G., & Matthews, K. 1988a, ApJL, 328, L35
Sanders, D. B., Soifer, B. T., Elias, J. H., et al. 1988b, ApJ, 325, 74
Smolčić, V., Capak, P., Ilbert, O., et al. 2011, ApJL, 731, L27
Soifer, B. T., Boehmer, L., Neugebauer, G., & Sanders, D. B. 1989, AJ, 98, 766
Stierwalt, S., Armus, L., Surace, J. A., et al. 2013, ApJS, 206, 1
Valiante, E., Lutz, D., Sturm, E., et al. 2007, ApJ, 660, 1060
Veilleux, S., Kim, D.-C., & Sanders, D. B. 2002, ApJS, 143, 315
Veilleux, S., Kim, D.-C., Sanders, D. B., Mazzarella, J. M., & Soifer, B. T. 1995, ApJS, 98, 171
Veilleux, S., Sanders, D. B., & Kim, D.-C. 1997, ApJ, 484, 92
Yun, M. S., Reddy, N. A., & Condon, J. J. 2001, ApJ, 554, 803
Yun, M. S., Scoville, N. Z., & Knop, R. A. 1994, ApJL, 430, L109
Zhu, M., Gao, Y., Seaquist, E. R., & Dunne, L. 2007, AJ, 134, 118